

# Characteristic Length of Energy-Containing Structures at the Base of a Coronal Hole

Abramenko, V.I.<sup>1</sup>, Zank, G.P.<sup>2</sup>, Dosch, A.<sup>2</sup>, Yurchyshyn, V.B.<sup>1</sup>, Goode, P.R.<sup>1</sup>, Ahn, K.<sup>1</sup>, Cao, W.<sup>1</sup>

<sup>1</sup> *Big Bear Solar Observatory, 40386 N. Shore Lane, Big Bear City, CA 92314, USA*

<sup>2</sup> *CSPAR, University of Alabama in Huntsville, Huntsville, AL, USA*

## ABSTRACT

An essential parameter for models of coronal heating and fast solar wind acceleration that rely on the dissipation of MHD turbulence is the characteristic energy-containing length  $\lambda_{\perp}$  of the squared velocity and magnetic field fluctuations ( $u^2$  and  $b^2$ ) transverse to the mean magnetic field inside a coronal hole (CH) at the base of the corona. The characteristic length scale defines directly the heating rate. We use a time series analysis of solar granulation and magnetic field measurements inside two CHs obtained with the New Solar Telescope (NST) at Big Bear Solar Observatory. A data set for transverse magnetic fields obtained with the Solar Optical Telescope/Spectro-Polarimeter (SOT/SP) aboard *Hinode* spacecraft was utilized to analyze the squared transverse magnetic field fluctuations  $b_t^2$ . Local correlation tracking (LCT) was applied to derive the squared transverse velocity fluctuations  $u^2$ . We find that for  $u^2$ -structures, Batchelor integral scale  $\lambda$  varies in a range of 1800 - 2100 km, whereas the correlation length  $\zeta$  and the  $e$ -folding length  $L$  vary between 660 and 1460 km. Structures for  $b_t^2$  yield  $\lambda \approx 1600$  km,  $\zeta \approx 640$  km, and  $L \approx 620$  km. An averaged (over  $\lambda$ ,  $\zeta$ , and  $L$ ) value of the characteristic length of  $u^2$ -fluctuations is  $1260 \pm 500$  km, and that of  $b_t^2$  is  $950 \pm 560$  km. The characteristic length scale in the photosphere is approximately 1.5-50 times smaller than that adopted in previous models ( $3-30 \times 10^3$  km). Our results provide a critical input parameter for current models of coronal heating and should yield an improved understanding of fast solar wind acceleration.

*Subject headings:* Sun: photosphere; surface magnetism; corona. Physical Data and Processes: turbulence

## 1. Introduction

Solar magneto-convection in the photosphere and beneath gives rise to a broad spectrum of magneto-hydrodynamic (MHD) waves, which carry energy (both kinetic and magnetic) from the

base of the solar corona into its outer parts. There is no doubt that the propagation, absorption, interaction and reflection of various types of MHD waves significantly contribute to the acceleration of solar wind (e.g. Matthaeus et al. 1999; Oughton et al. 1999; Thomas & Stanchfield 2000; Dmitruk et al. 2001; Bogdan et al. 2003; Cranmer & van Ballegoijen 2005; Cranmer et al. 2007; Verdini et al. 2010; Zank et al. 2012, to mention a few). To account for turbulent dissipation of MHD waves, a solution to the dissipative MHD equations is required, i.e., the dissipative term should be incorporated. The dissipative term, in turn, depends on a "free" parameter, namely, the characteristic energy-containing length  $\lambda_{\perp}$  of the dynamical structures transverse to the mean magnetic field in a coronal hole (CH) at the base of the corona, where the fast solar wind is emanated (e.g. Matthaeus et al. 1999; Oughton et al. 1999; Dmitruk et al. 2001; Cranmer & van Ballegoijen 2005; Zank et al. 2012). The turbulent dissipation rate, responsible for heating and solar wind acceleration, is inversely proportional to  $\lambda_{\perp}$ , see Eq (8) in Dmitruk et al. (2001), Eq. (56) in Cranmer & van Ballegoijen (2005) and Eq. (16) in Zank et al. (2012).

The characteristic energy-containing length scale is an integral element underlying the decomposition of MHD fluctuations into high- and low-frequency components (Matthaeus et al. 1999; Zank et al. 2012). Indeed, within the existing models that exploit the dissipation of low-frequency turbulence to heat the solar corona,  $\lambda_{\perp}$  plays perhaps the key role in determining efficiency of heating. Rather surprisingly, almost nothing is known observationally about this critical parameter. Currently, only a very rough estimate of  $\lambda_{\perp}$  was obtained based on the fact that the network spacing is about  $3 \times 10^4$  km (or an order of magnitude less, Matthaeus et al. 1999; Dmitruk et al. 2001). Cranmer & van Ballegoijen (2005) introduced parametrized  $\lambda_{\perp}$ , which could be translated into 3 Mm near the base of the corona.

The goal of this work is to provide a better estimate for the energy-containing length scales using observed data on the transverse velocities and magnetic fields at the coronal base of a CH. We will analyse energy-containing structures of  $u^2 = u_x^2 + u_y^2$  and  $b_t^2$ , where  $u_x$ , and  $u_y$  are the transverse velocities, and  $b_t$  is the transverse component of the magnetic field in the photosphere inside a CH. Only for the purposes of comparison, the line-of-sight (LOS) component of the magnetic field is also analysed.

## 2. Data

We utilize data from the 1.6 m clear aperture New Solar Telescope (NST, Goode et al. (2010)) operated at the Big Bear Solar Observatory. High time cadence sequences of solar granulation images allowed us to calculate squared transverse velocities at the photospheric level ( $\tau_{500} = 1$ ), whereas the co-temporal and co-spatial near-infrared magnetograms from the NST provided us with the LOS magnetic fields inside CHs. The squared transverse magnetic field

fluctuations  $b_t^2$  analyzed here were obtained from the Spectro-Polarimeter data at the Solar Optical Telescope (SOT/SP) aboard *Hinode* spacecraft (Kosugi et al. 2007; Tsuneta et al. 2008) acquired on 2007 March 10.

Two CHs for which NST time series were obtained are shown in Figure 1. Both CHs were observed at the times of their crossing the central meridian. The first CH was observed on 2011 August 12, and it is referred to hereafter as CH 2011-08-12. It was observed for nearly 20 minutes with a field of view (FOV,  $56'' \times 56''$ ). The second CH was observed with a FOV of  $31'' \times 28''$  during about 2 hours on 2012 June 4 and is referred to hereafter as CH 2012-06-04.

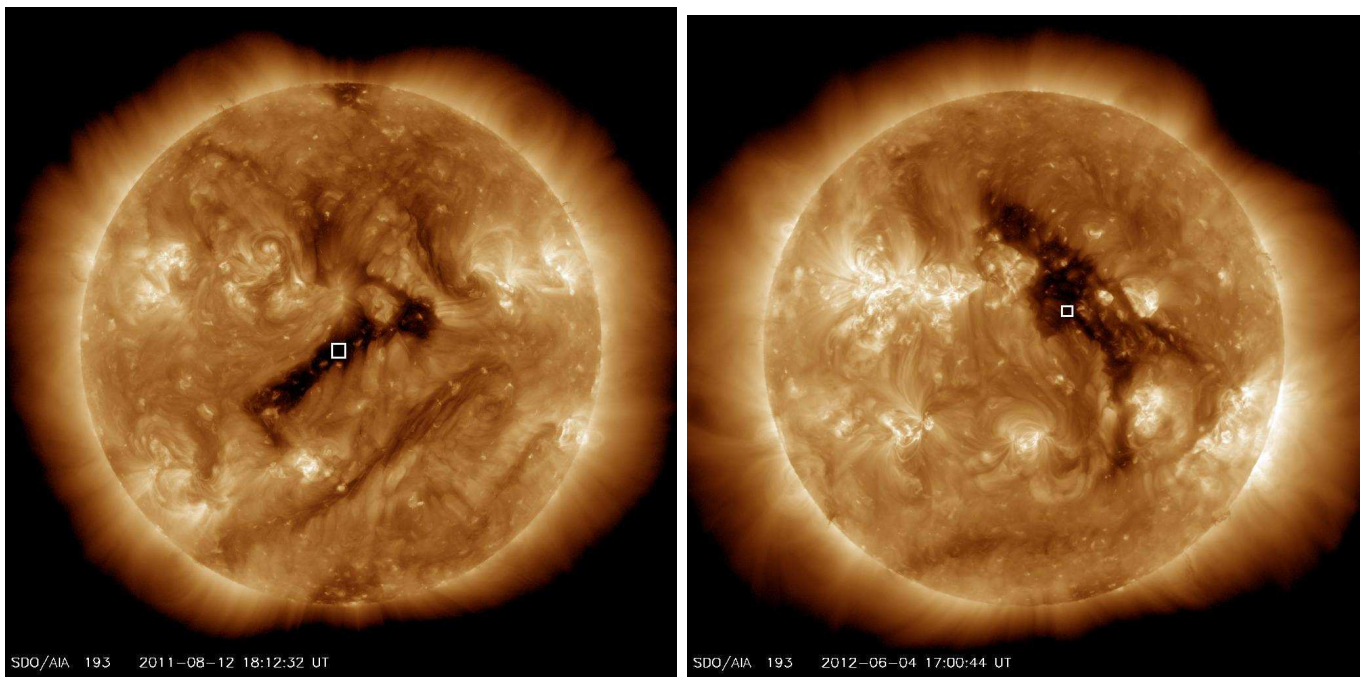


Fig. 1.— SDO/AIA/193Å images showing the location of the two CHs observed on 2011 August 12 (left) and 2012 June 4 (right). The white boxes indicate the location of the NST FOV.

The solar granulation data were acquired with a broad-band TiO filter centered at 705.7 nm with a band-pass of 1 nm (for details see Abramenko et al. 2012). The observations were aided with an adaptive optics (AO) system (Denker et al. 2007; Cao et al. 2010). To take maximal advantage of the AO system, only the central part of the entire FOV ( $77'' \times 77''$ ) was utilized. The pixel scale of the PCO.2000 camera,  $0.''0375$ , was 2.9 times smaller than the telescope diffraction limit of 77 km. The Kiepenheuer-Institut für Sonnenphysik’s software package for speckle interferometry (KISIP, Wöger & von der Lühe 2007) was applied to the 70 best images selected from a burst of 100 images to produce one speckle reconstructed image at the diffraction

limited resolution. After destretching and sub-sonic filtering (Abramenko et al. 2011) of speckle reconstructed images, the final CH 2011-08-12 (CH 2012-06-04) data set consisted of 82 (659) images. The final time cadence was 12 and 13 s, respectively. One-two minutes gaps are sometimes present in the data. An example of a TiO/NST image of granulation is shown in Figure 2 (left).

Spatial fluctuations of the *transverse* component of the magnetic field inside a CH are of primary interest in this paper. Unfortunately, these kind of data are less plentiful, and the accuracy of measurements is much lower than that for the line-of-sight (LOS) data, especially in the quiet sun and in coronal holes. With this in mind, we address the problem in the following way. We utilized Hinode/SOT/SP data acquired inside a quiet sun region at the solar disk center on 2007, March 10. The processed data of the magnitude of the transverse magnetic field  $B_{app}^T$  and the corresponding LOS magnetic field  $B_{app}^L$  were kindly provided to us by Dr. B. Lites. The SOT/SP slit scanned an area of  $304'' \times 164''$ , or  $220 \times 120$  Mm. The pixel size was  $0.''150 \times 0.''160$ . The data acquisition, processing and noise issues are described in detail by Lites et al. (2008). The maps of the magnetic field components are shown in their Figure 2. We consider the  $B_{app}^T$  data set as the primary source for deriving the characteristic length of the transverse magnetic fluctuations. For comparison, we also calculated the  $\lambda$ ,  $\zeta$ , and  $L$  from the LOS component  $B_{app}^L$ .

We also utilized LOS magnetograms obtained for CH 2012-06-04 with the near-infrared imaging magnetograph (IRIM, Cao et al. 2010) installed on the NST. The spectro-polarimeter uses the Fe I spectral line at  $1.56 \mu\text{m}$  and is based on a 2.5 nm interference filter, a  $0.25 \text{ \AA}$  birefringent Lyot filter (Wang et al. 2000), and a Fabry-Pérot etalon and provides a bandpass of  $\sim 0.01 \text{ nm}$  over a FOV of  $50'' \times 25''$  with a pixel scale of  $0.''098$ . Based on the advantages of the near IR window and the NST adaptive optics, IRIM provides solar spectro-polarimetry data with Zeeman sensitivity of  $10^{-3} I_c$ , diffraction limited resolution of  $0.''2$ , and time cadence of 45 s (for full Stokes profiles). The raw IRIM data were processed to take into account dark and flat field corrections and polarization calibration (Cao et al. 2010; Goode et al. 2011; Cao et al. 2011). The linear polarization signal (the source of the transverse magnetic field data) from IRIM is very weak in CHs, therefore noise issues precluded scientific usage of it, while the LOS magnetic field component was reliably derived by using the weak-field approximation. The best 34 LOS magnetograms (Figure 2, right) were utilized here to estimate the characteristic length of  $b_z$ .

### 3. Transverse Velocities Acquisition

To derive transverse velocities in the photosphere, we applied the Local Correlation Tracking (LCT) routine to the time series of solar granulation. The routine was first proposed by November & Simon (1988) and later modified and improved (e.g., Title et al. 1995; Hurlburt et al.

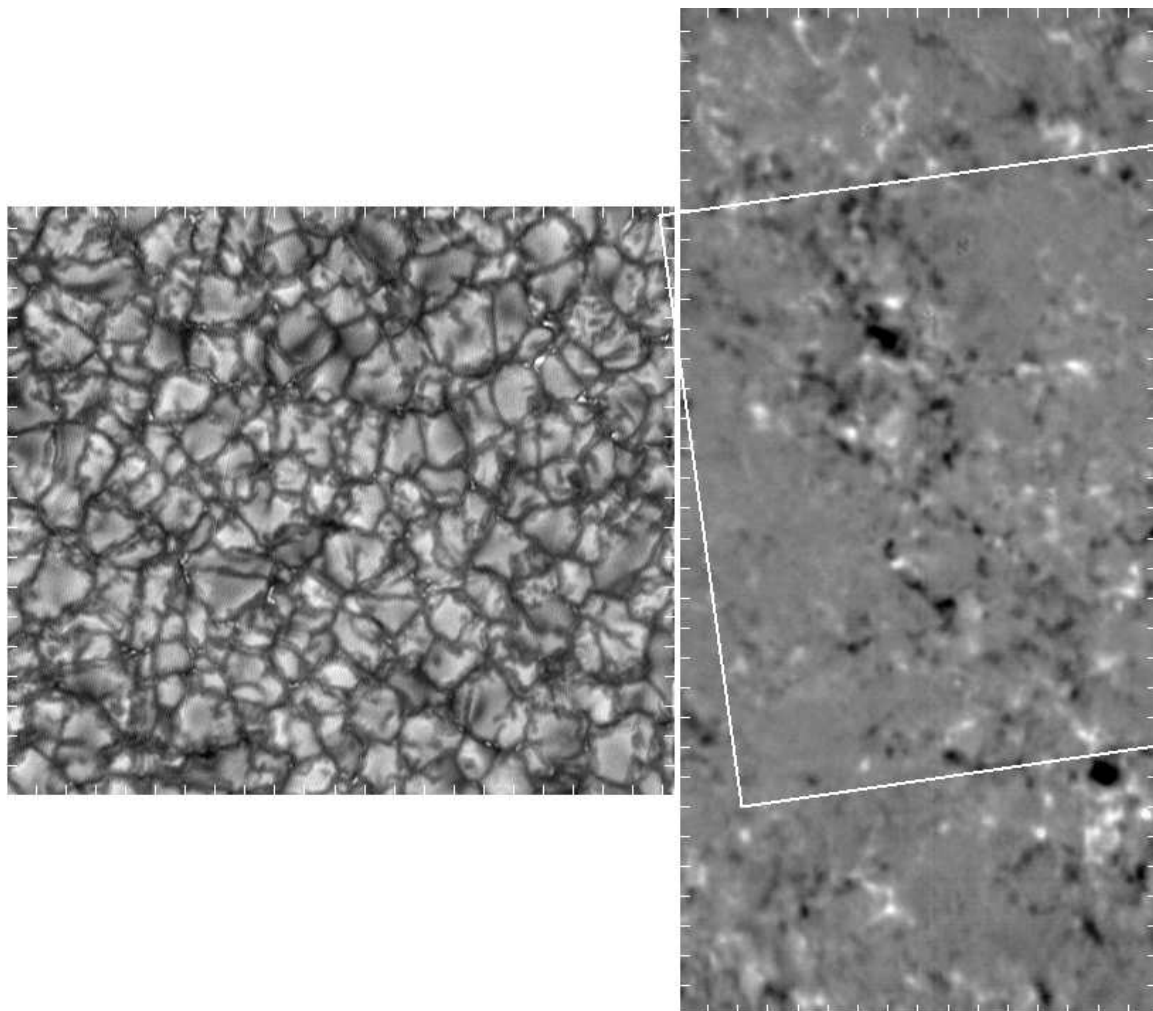


Fig. 2.— Left - one of the 659 images of CH 2012-06-04 obtained with the NST/TiO filter. Right - the co-temporal NST/IRIM LOS magnetogram. The white lines outline three boundaries of the FOV/TiO. The magnetogram is scaled from -100 G (black) to 100 G (white). The magnetogram and the granulation are shown in the same scale. The ticks separate a distance of 1 Mm.

1995; Strous et al. 1996; Welsch et al. 2007; Chae & Sakurai 2008; Matloch et al. 2010; Verma & Denker 2011; Verma et al. 2013).

Matloch et al. (2010) tested the performance of the LCT on simulated data for quiet-sun granulation. The used LCT code is described in Welsch et al. (2007). The authors found that the LCT-derived velocities were approximately two times smaller than those derived directly from the simulations. The agreement between the simulated and LCT velocities was found to depend on the depth in the simulation box. The correlation reaches maximum ( $\sim 0.65$ ) at the depth close

to the optical depth of  $\tau = 1$ , i.e., near the continuum formation level.

Verma & Denker (2011) and Verma et al. (2013) presented a comprehensive study of accuracy and reliability of the LCT technique by applying it to *Hinode* G-band images. They demonstrated (Verma & Denker 2011) that the choice of three essential input parameters (time cadence,  $\delta t$ , accumulation interval,  $T$ , and the FWHM of a Gaussian sampling window,  $W$ ) may significantly affect the result. Verma et al. (2013) evaluated the LCT technique using CO5BOLD simulations of solar granulation (Freytag et al. 2012). Note, that the spatial and temporal resolution (28 km pixel scale and 10 s lowest time cadence) of the simulated data set are comparable to those of the observed NST set analyzed here (27 km pixel scale and 12-13 s time cadence). Verma et al. (2013) found that, when multiplied by a factor of three, the frequency distribution of the LCT velocities demonstrates a very good agreement with the distribution of the velocities derived directly from the simulated set (see Figure 13 in Verma et al. 2013). Furthermore, Figure 7 in Verma et al. (2013) suggests that the time cadence of 10-30 s and the apodization window of 600-1000 km are the best choice for analysis of the inter-granular dynamics. Interestingly, the narrower window of 400 km results in diminishing of the LCT velocities and degradation of the fine structures in the velocity pattern, so that the LCT technique fails to capture the inter-granular dynamics there.

Figures 4 - 6 in Verma et al. (2013), as well as Figure 3 in Verma & Denker (2011) demonstrate that the extension of the accumulation interval  $T$  results in diminishing of the LCT velocities as well. The authors found that in order to reveal the persistent (e.g., meso- granular and/or super-granular) flows in the solar granulation, the accumulation time should be no less than approximately 20 minutes. One might conclude that shorter time intervals should be employed to reveal inter- granular dynamics.

Here we focus on analysis of inter-granular dynamics, i.e., on proper motions of granule edges, mini-granules (Abramenko et al. 2012), inter-granular bright points (BPs) and filigree-like features. According to MHD simulations (Stein 2013) and NST observations, these features visible inside inter-granular lanes are mostly associated with strong quiet Sun magnetic fields. It is thought that Alfvén waves are generated by rapid displacements of magnetic footpoints driven by these inter-granular flows and the energy-containing scale should be related to this kind of motions. We will choose the LCT configuration parameters based on the above considerations and the results of Verma & Denker (2011) and Verma et al. (2013).

The version of the LCT used here was elaborated by Strous (1994) and Strous et al. (1996) and it is utilizing ANA software package <sup>1</sup>. We start with choosing the best time cadence  $\delta t$  using the CH-2012-06-04 data recorded with time cadence of 13 s. We generated two additional

---

<sup>1</sup>see more at <http://ana.lmsal.com/ana/>

sets with  $\delta t \approx 39$  and 65 s by selecting each third and fifth image, respectively. In this case, with  $T = 10$  min and  $W = 540$  km, we obtained the following values of the square root of the averaged squared velocities:  $1.21 \text{ km s}^{-1}$  for  $\delta t = 13$  s,  $0.61 \text{ km s}^{-1}$  for  $\delta t = 39$  s, and  $0.26 \text{ km s}^{-1}$  for  $\delta t = 65$  s. We thus concluded that the first estimate of the LCT velocity ( $1.21 \text{ km s}^{-1}$  derived for  $\delta t = 13$  s) is the best choice because it is the largest one out of the three and the closest one to the estimates derived by Verma et al. (2013, see Figure 8) for the range of  $\delta t = 10\text{-}30$  s and  $W = 600\text{-}1000$  km.

The next critical parameter is the FWHM of the Gaussian sampling window  $W$ . According to Verma & Denker (2011) and Verma et al. (2013), the choice of  $W$  must be guided by the spatial scales of the studied dynamic events. In case of the inter-granular scale events, the window should not exceed the typical size of a granule, i.e.,  $\sim 1000$  km. We thus tested three choices of  $W$ :  $10 \times 10$  pixels (270 km in linear extent),  $20 \times 20$  pixels (540 km), and  $40 \times 40$  pixels (1090 km) for which we obtained the following square root of the averaged squared velocities:  $1.02 \text{ km s}^{-1}$  for  $W = 270$  km,  $1.21 \text{ km s}^{-1}$  for  $W = 540$  km, and  $1.11 \text{ km s}^{-1}$  for  $W = 1090$  km. Again, we chose the  $W = 540$  km value since it ensures the largest detected velocities.

Finally, the accumulation (averaging) time interval  $T$  should be shorter than 20 minutes. Similarly, four choices of  $T$  were tested: 2, 5, 10, and 20 min. The following square root of the averaged squared velocities were obtained: 1.71, 1.40, 1.21, and  $1.06 \text{ km s}^{-1}$ , respectively. Qualitatively, the tendency here agrees with that reported by Verma & Denker (2011) and Verma et al. (2013): the averaged velocity decreases as  $T$  increases. However, there is no indication which one might be closer to the real value. The possible answer is that all of them are true, and they simply reflect the dynamics on different time scales. We, therefore, decided to proceed using all of the above accumulation intervals.

As we saw above, underestimation of the LCT velocities by 2 to 3 times is an unavoidable shortcoming of the LCT technique. However, in this particular study, we are focused on calculation of the correlation functions characterizing LCT velocities structures rather than on the magnitude of the velocities. According to the general expression of the correlation function (see Eq.1 below), multiplying the velocity (or squared velocities) by a constant factor does not change the correlation function (the factor evenly appears in the numerator and the denominator of the right-hand part of Eq. 1).

Note, that the TiO spectral line is formed in the quiet sun at optical depths of  $\tau = 1$ , i.e., near the continuum level (Abramenko et al. 2012; Berdyugina et al. 2003), where the LCT is expected to perform in the most reliable way (Matloch et al. 2010).

#### 4. Different Methods to Derive the Characteristic Length

Our main goal is to find, following Batchelor (1953), "convenient measures of the linear extent of the region within which velocities [as well as squared velocities and magnetic field] are appreciably correlated". For an arbitrary two-dimensional scalar field  $v(\mathbf{r})$ , a general definition of the correlation function  $B(\mathbf{r})$  reads as (Jenkins & Watts 1969; Monin & Yaglom 1975)

$$B(r) = \langle (v(\mathbf{x} + \mathbf{r}) - \langle v \rangle) \cdot (v(\mathbf{x}) - \langle v \rangle) \rangle / \sigma^2, \quad (1)$$

where  $\mathbf{r}$  is a separation vector,  $\mathbf{x} \equiv (x, y)$  is the current point on an image, and  $\sigma^2$  is the variance of  $v$ . Angle brackets denote averaging over the area of an image. Based on  $B(\mathbf{r})$ , the characteristic length of the field  $v$  can be defined as a distance where some correlation in  $v$  holds.

We will use three different approaches for deriving the characteristic length from the correlation function  $B(r)$ . For a noise-free smooth image, measured on a large enough area, all of our approaches produce the same magnitude for the characteristic length. However, in case of real data, the estimates from different methods might differ. We will consider the results obtained from these approaches as independent estimates of the characteristic length for a given image.

The first approach is to determine the integral scale (Batchelor 1953)

$$\lambda = \int_0^{r_{max}} B(r) dr, \quad (2)$$

which has also been used in the formulation/derivation of the turbulence transport model of Zank et al. (2012). Here the integration is supposed to be performed over all scales up to infinity. However, in the case of real data, at scales exceeding a certain large distance, data noise might cause a non-diminishing  $B(\mathbf{r})$ , thus resulting in an artificially large integral scale. To mitigate this problem, the signal in pixels was assigned to be zero when the absolute value of the measured signal was below one standard deviation. Moreover, we noticed that in our data sets an increase in correlation is observed at scales larger than approximately 5 Mm, which is caused by the presence of adjacent features in a studied field. To avoid an overestimation of the integral length, we adopted  $r_{max}$  in Eq. 2 to be 5 Mm.

The second method is to approximate the correlation function near the origin (Hinze 1959; Monin & Yaglom 1975; Feder 1989):

$$B(r) = Const \cdot \exp(-r/\varsigma). \quad (3)$$

Thus, when  $B(r)$  is fitted with an exponential function, the correlation function drops by  $e$  times at a scale  $\varsigma$ . This scale is called the correlation length in the percolation (Feder 1989) and in second-order phase transition <sup>2</sup> theories.

---

<sup>2</sup> <http://staff.science.nus.edu.sg/~parwani/c1/node52.html>



Finally, the characteristic length can also be determined via the  $e$ -folding scale of  $B(r)$  without any approximation of the latter (the scale, where the *measured* correlation function drops by  $e$  times). We denote this measure as  $L$ .

The parameters introduced above  $\lambda$ ,  $\varsigma$ , and  $L$  are considered as proxies for the characteristic length, and were calculated for all data sets.

## 5. Results

### 5.1. Characteristic Length of Transverse Velocity Fluctuations

Dividing the resulting LCT displacements in each pixel by the accumulation time  $T$ , we obtained components of the transverse velocities  $U_x$  and  $U_y$  (flow maps). We then computed the probability distribution functions (PDFs, Figure 3) of  $U_x$  and  $U_y$  for each flow map, which showed that alignment of the images in the data sets was very good, and there are no large-scale systematic shifts, so that residual large-scale velocities (mean velocities) are negligible. Indeed, the PDFs of the  $U_x$  and  $U_y$  components are well centered at zero and are distributed in accordance with a Gaussian function. The mean velocity components  $\langle U_x \rangle$  and  $\langle U_y \rangle$  do not exceed  $35 \text{ m s}^{-1}$  in any flow map. After subtraction of the mean velocities from the flow maps, we obtained the velocity fluctuations maps  $u_x$  and  $u_y$ . A fragment of a  $u_x, u_y$ -map is shown in Figure 4, *left*. Centers of large granules are usually places of slow transverse motions, whereas the majority of long arrows are located near the periphery of large granules and inside inter-granular lanes, thus supporting the idea of enhanced dynamics in inter-granular lanes and proving the capability of the LCT to detect it.

We first focus on the statistical properties of the squared amplitude  $u^2 = (u_x^2 + u_y^2)$  of the  $(u_x, u_y)$ -vector, which is a positive scalar that characterizes the kinetic energy of photospheric random motions driven by convection and turbulence. Therefore, the  $u^2$ -maps represent an entity in which we are interested (see Eqs. 2-6 in Zank et al. (2012)). In the right panel of Figure 4, we show a  $u^2$ -map calculated from the flow map shown in the left panel. Patches of enhanced kinetic energy (white areas) are intermittent with dark voids. Our aim is to estimate the characteristic length of these patches.

Figure 5 shows the correlation functions of  $u^2$  structures determined with different accumulation intervals  $T$ . All the proxies of the characteristic length  $\lambda$ ,  $\varsigma$ , and  $L$  (see Sec. 4) show an increase with larger  $T$ , which seems to be expected because various small-scale velocity patterns tend to be smeared as they are averaged over time longer time intervals (Table 1.) The estimate of the Batchelor integral length  $\lambda$  is the largest. For all cases,  $\varsigma$  is less than  $L$ . Based on the three proxies, the characteristic length of  $u^2$  varies in the range of 660 - 2130 km with an average

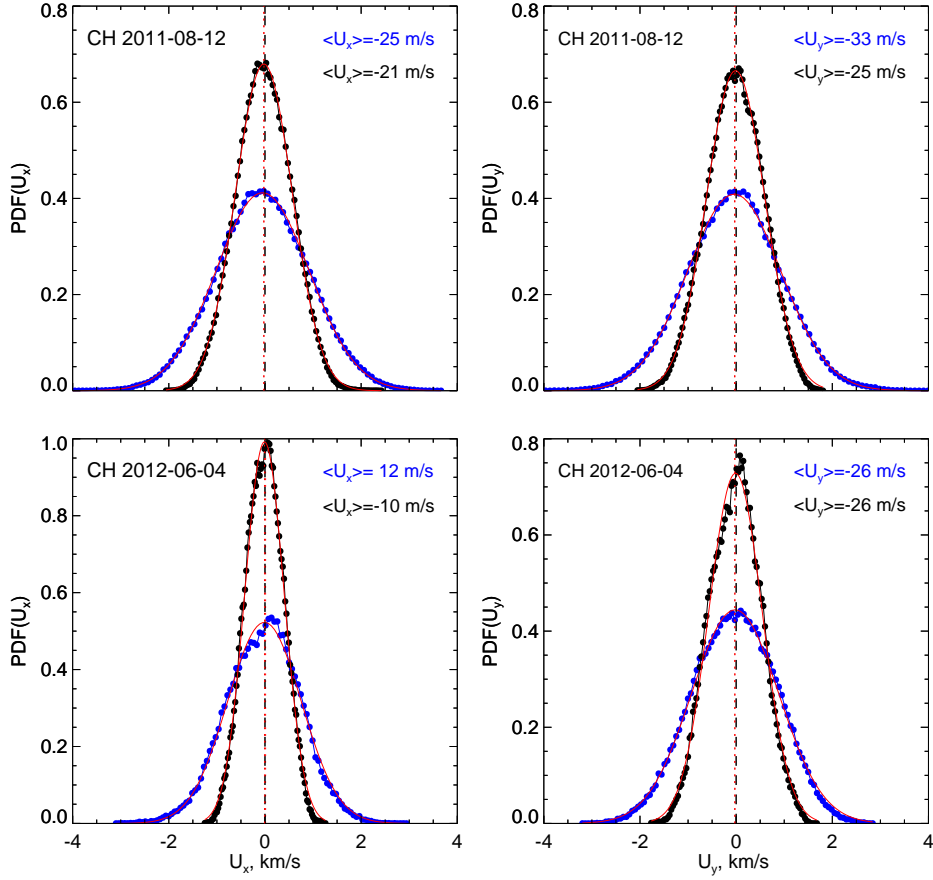


Fig. 3.— Probability distribution functions (PDFs) of the transverse velocities,  $U_x$  (left) and  $U_y$  (right) derived from a velocity map for CH 2011-08-12 (top, 734 x 734 data points) and CH 2012-06-04 (bottom, 351 x 351 data points). PDFs, obtained with the accumulation time interval  $T = 2$  (20) min are shown with blue (black) circles. The red curves are the best Gaussian fit to the data points. The mode of the Gaussian fit is shown for each data set with the same color code. The Gaussian mode deviates from zero by less than  $35 \text{ m s}^{-1}$  for all flow maps.

value of  $1260 \pm 500 \text{ km}$ .

We then calculated correlation functions of the transverse velocity components  $u_x$  and  $u_y$ . For a 2D vector field (unlike a scalar field), one has to compute two correlation functions (Batchelor 1953): one of them,  $B_p$ , is parallel to the separation vector  $\mathbf{r}$ , and the other one,  $B_n$ , is normal to  $\mathbf{r}$ . To simplify the calculations without sacrificing the quality, we computed  $B_p(u_x)$  assuming that  $r$  varies along the  $x$ -axis only.  $B_n(u_x)$  was computed with  $r$  varying along

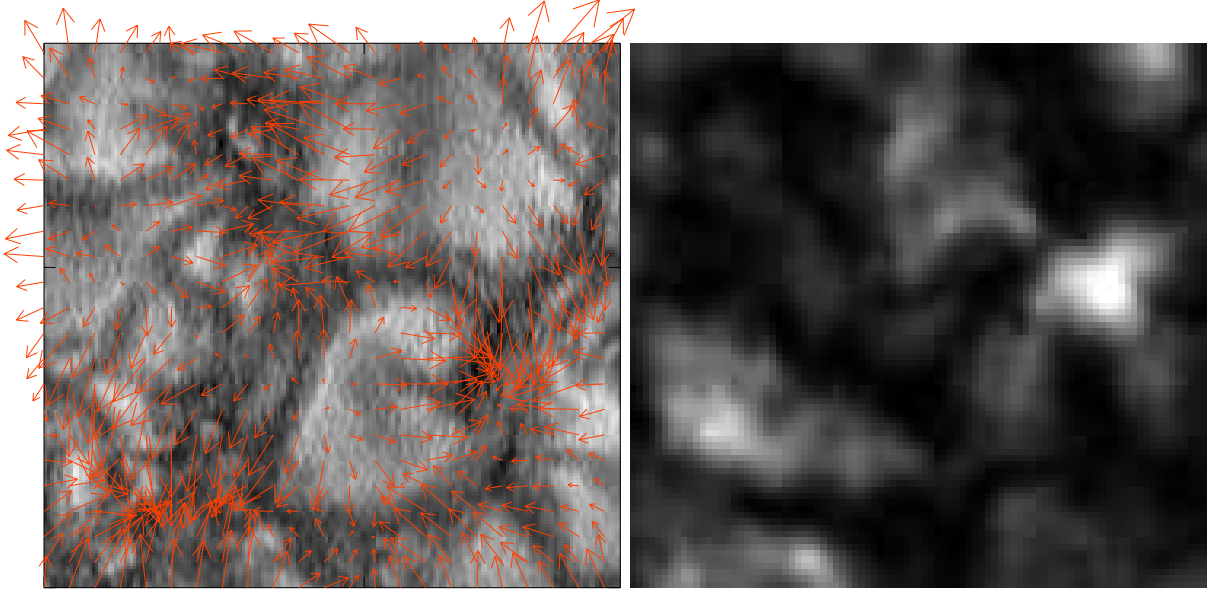


Fig. 4.— *Left* - NST/TiO image of solar granulation inside CH 2012-06-04 overplotted with the corresponding velocity fluctuations map (arrows) obtained with  $T = 10$  min. The image size is  $4.9 \times 4.6$  Mm. The length of the arrows is in proportion to the velocity, and the longest arrows correspond to  $2.2 \text{ km s}^{-1}$ . *Right* - the corresponding map of squared transverse velocity fluctuations,  $u^2$ , saturated at  $4 \text{ km}^2 \text{ s}^{-2}$ .

Table 1: Characteristic lengths of the squared transverse velocity fluctuations,  $u^2$

	$\lambda$ , km	$\varsigma$ , km	$L$ , km
CH 2011-08-12			
$T = 2$ min	1820	660	840
$T = 5$ min	1850	700	880
$T = 10$ min	1970	840	1080
$T = 20$ min	2130	1020	1460
CH 2012-06-04			
$T = 2$ min	1770	660	850
$T = 5$ min	1810	760	970
$T = 10$ min	1860	890	1080
$T = 20$ min	1940	1070	1260
$\langle \lambda_{\perp} \rangle$	$1890 \pm 120$	$830 \pm 160$	$1050 \pm 220$

the  $y$ -axis. The correlation functions for  $u_x$  are shown in Figure 6. Similarly, we computed both correlation functions for  $u_y$ , which were very similar to that derived for  $u_x$ , so their plots are not shown. Obtained from the plots averaged (over  $T$  and both CHs) values of  $\lambda$ ,  $\varsigma$ , and  $L$  are

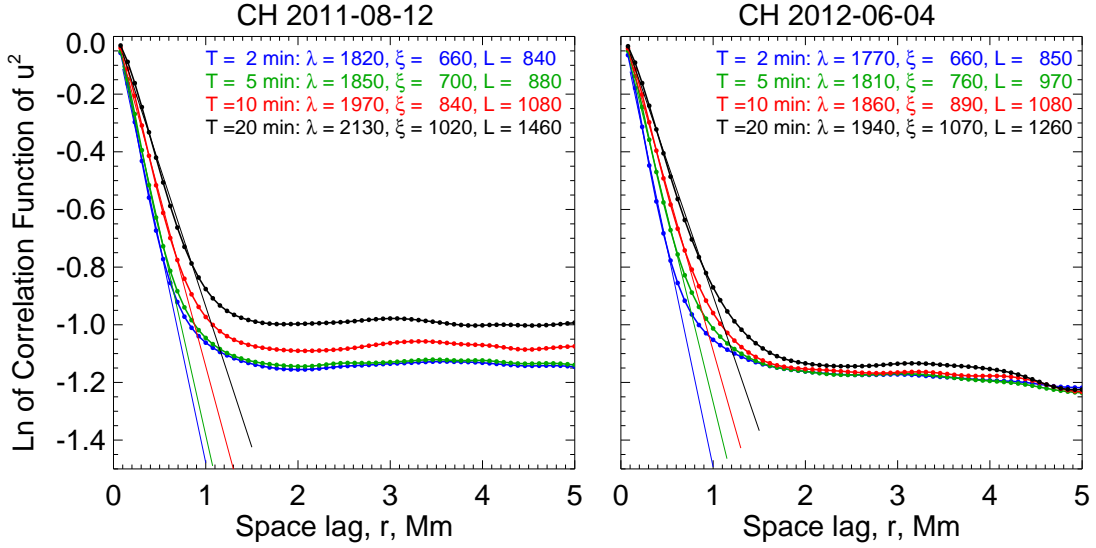


Fig. 5.— Plotted is the natural logarithm of the correlation function of  $u^2$  versus the spatial lag  $r$  for the two CHs. The circles denote the data points and the straight lines are best linear fits to the first 8-10 data points used to derive  $\zeta$  according to Eq. 3. The color code refers to the accumulation time intervals of 2 (blue), 5 (green), 10 (red), and 20 (black) minutes. The values of the integral length  $\lambda$  the correlation length  $\zeta$  and the  $e$ -folding length  $L$  in km are shown.

gathered in Table 2.

Table 2: Averaged characteristic lengths of the components  $u_x$  and  $u_y$  from the parallel  $B_p(r)$  and normal  $B_n(r)$  correlation functions

	$\lambda$ , km	$\zeta$ , km	$L$ , km	$\lambda$ , km	$\zeta$ , km	$L$ , km
	$u_x$			$u_y$		
$\langle \lambda_{\perp} \rangle$ for $B_p(r)$	$650 \pm 100$	$840 \pm 140$	$830 \pm 120$	$800 \pm 190$	$860 \pm 160$	$850 \pm 140$
$\langle \lambda_{\perp} \rangle$ for $B_n(r)$	$1340 \pm 230$	$1240 \pm 290$	$1260 \pm 300$	$1430 \pm 250$	$1270 \pm 320$	$1300 \pm 320$

The averaged integral length  $\lambda$  derived for both CHs using  $u_x$  and  $u_y$  from the parallel correlation functions  $B_p(u_x), B_p(u_y)$  is  $720 \pm 160$  km, whereas  $\lambda$  calculated from the normal correlation functions is  $1380 \pm 230$  km. Both are smaller than  $\lambda$  obtained from  $B(u^2)$ . This can be understood from the non-negative nature of the  $u^2$  field which gives an extended positive tail for  $B(u^2)$ . This is not the case for the parallel and normal correlation function of the alternating-sign fields of  $u_x$  and  $u_y$ . The correlation length  $\zeta$  and the  $e$ -folding length  $L$  from  $u_x, u_y$  agree within the error bars with that derived from  $u^2$ .

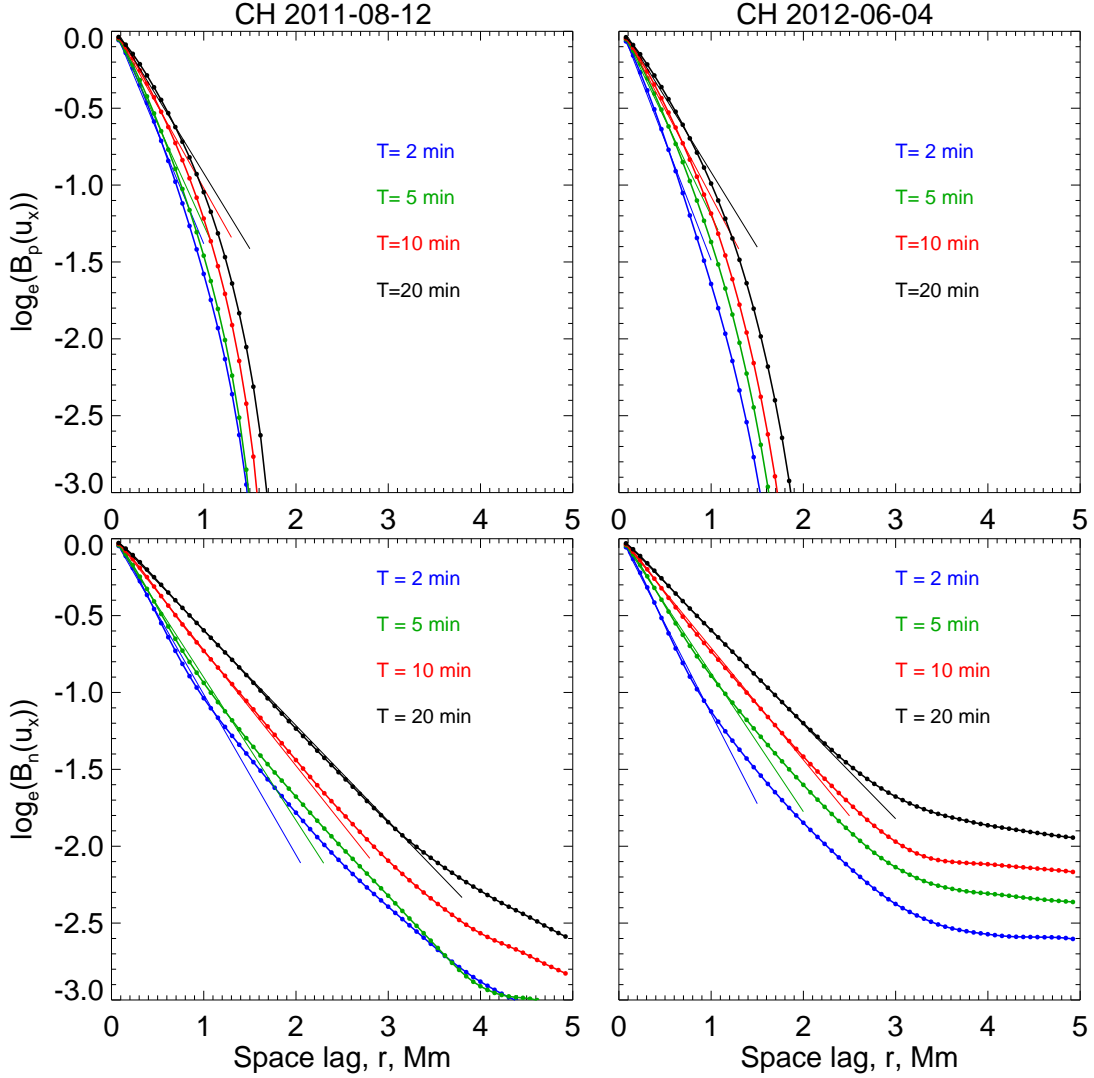


Fig. 6.— Plotted is the natural logarithm of the parallel (upper row) and normal (bottom row) correlation functions for  $u_x$  versus the spatial lag  $r$ . The notation is the same as in Figure 5.

We find that the behaviour of the parallel and normal correlation functions is different (see Figure 7). Whereas the normal correlation function  $B_n$  is positive for all scales, the parallel function changes sign, always situated below the normal correlation function; i.e.,  $B_p(r) < B_n(r)$ . This situation holds for all the analysed data sets and for both velocity components  $u_x$  and  $u_y$ . On average, the parallel correlation function has a characteristic length of  $800 \pm 160$  km, whereas the characteristic length derived from the normal correlation function is  $1310 \pm 280$  km. Note

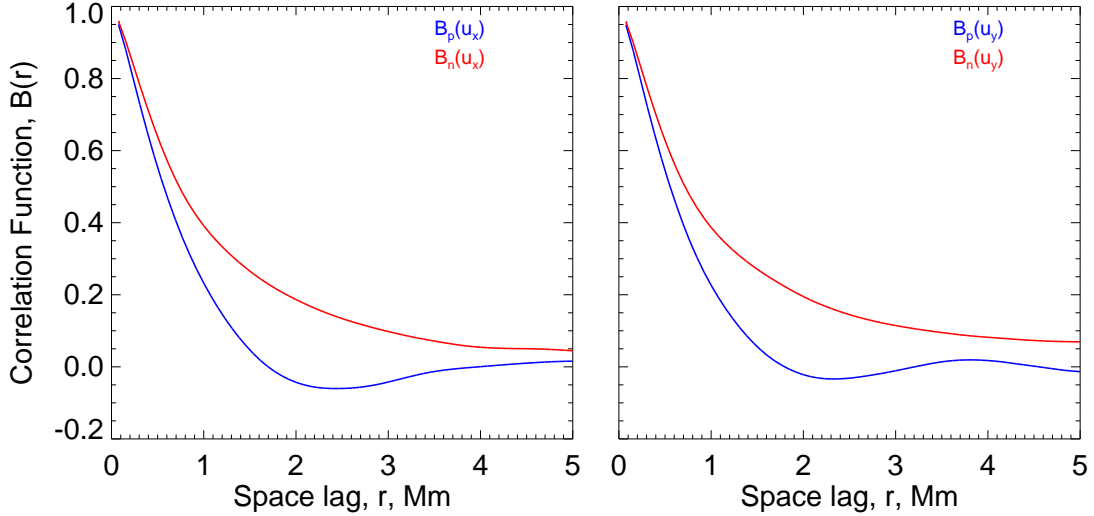


Fig. 7.— An example of the parallel (blue) and normal (red) correlation functions calculated from  $u_x$  (left) and  $u_y$  (right) components of the transverse velocity fluctuations. The data for CH-2011-08-12 obtained with the accumulation time of  $T = 5$  min are used for these plots.

that in the case of homogeneous isotropic hydro-dynamical turbulence, the mutual behavior of the parallel and normal correlation functions of velocity fluctuations is expected to be quite the opposite, i.e., the parallel correlation function exceeds the normal correlation function at all scales:  $B_p(r) > B_n(r)$  (Batchelor 1953; Monin & Yaglom 1975). Obviously, the condition of homogeneous isotropic turbulence is not met in the solar photosphere. Moreover, the presence of magnetic fields could also contribute in the observed peculiar relationship between the correlation functions.

## 5.2. Characteristic Length of the Magnetic Field Fluctuations

The correlation functions from the squared magnetic field components are shown in Figure 8. The most interesting to us is the correlation function of the squared transverse magnetic field component  $b_t^2$  plotted with the green line. On scales below approximately 0.5 Mm, the three correlation functions are similar. On larger scales, the NST  $b_z^2$  function (red line) agrees well with that derived from  $b_t^2$ . (The estimates for  $\lambda$ ,  $\zeta$ , and  $L$  derived from the green and red curves are similar too.) It is plausible that the very low noise level in the  $B_{app}^L$  data (about 2-3 Gauss, Lites et al. 2008) is the reason why on scales larger than 1 Mm the blue curve in

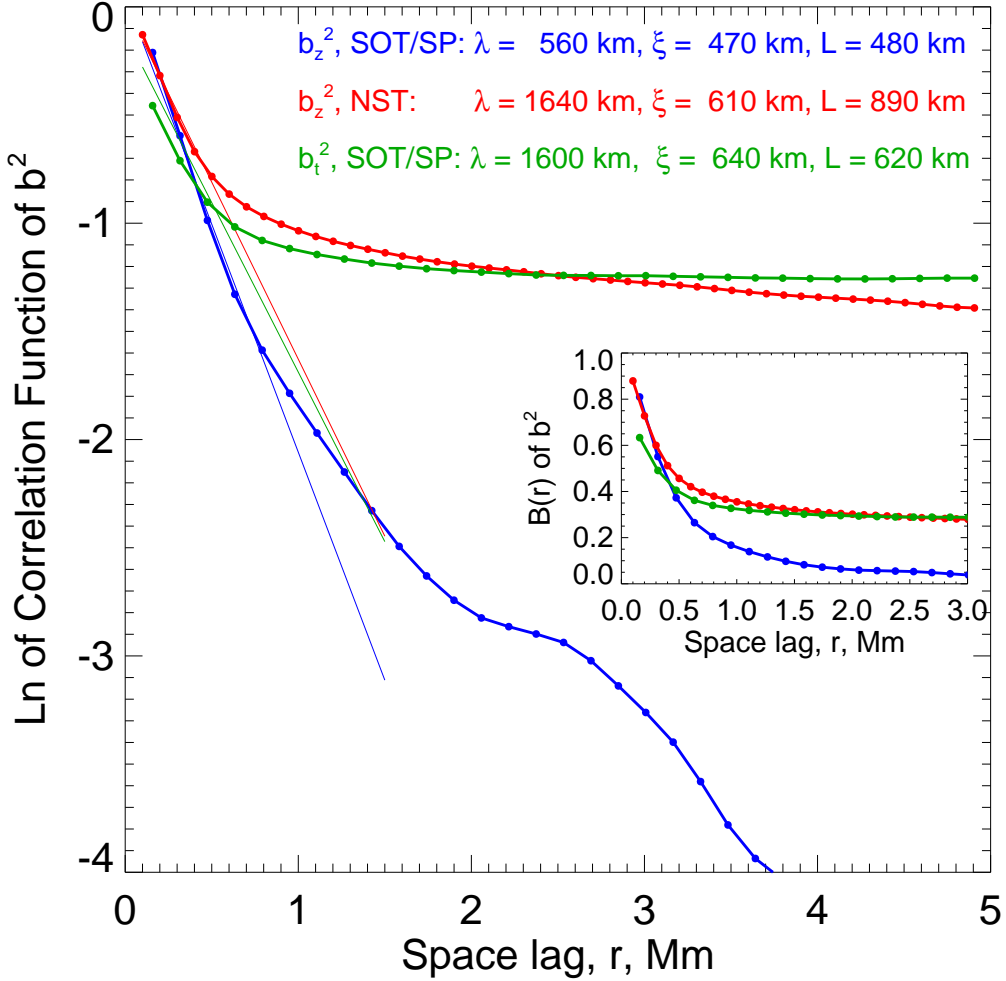


Fig. 8.— Plot of the natural logarithm of the correlation function of  $b^2$  versus the spatial lag  $r$ . Circles denote the data points, and the straight lines are the best linear fits to the first data points used to derive the values of  $\zeta$  from Eq. 3. The insert shows this plot with linear axes.

Figure 8 is much lower than the green and red curves. Thus, the correlation functions from the squared LOS component of the magnetic field can be used as an appropriate proxy to estimate the the correlation function of the squared transverse component. The characteristic length of the squared transverse magnetic field fluctuations varies in a range of 617 - 1600 km with an average value of  $950 \pm 560$  km.

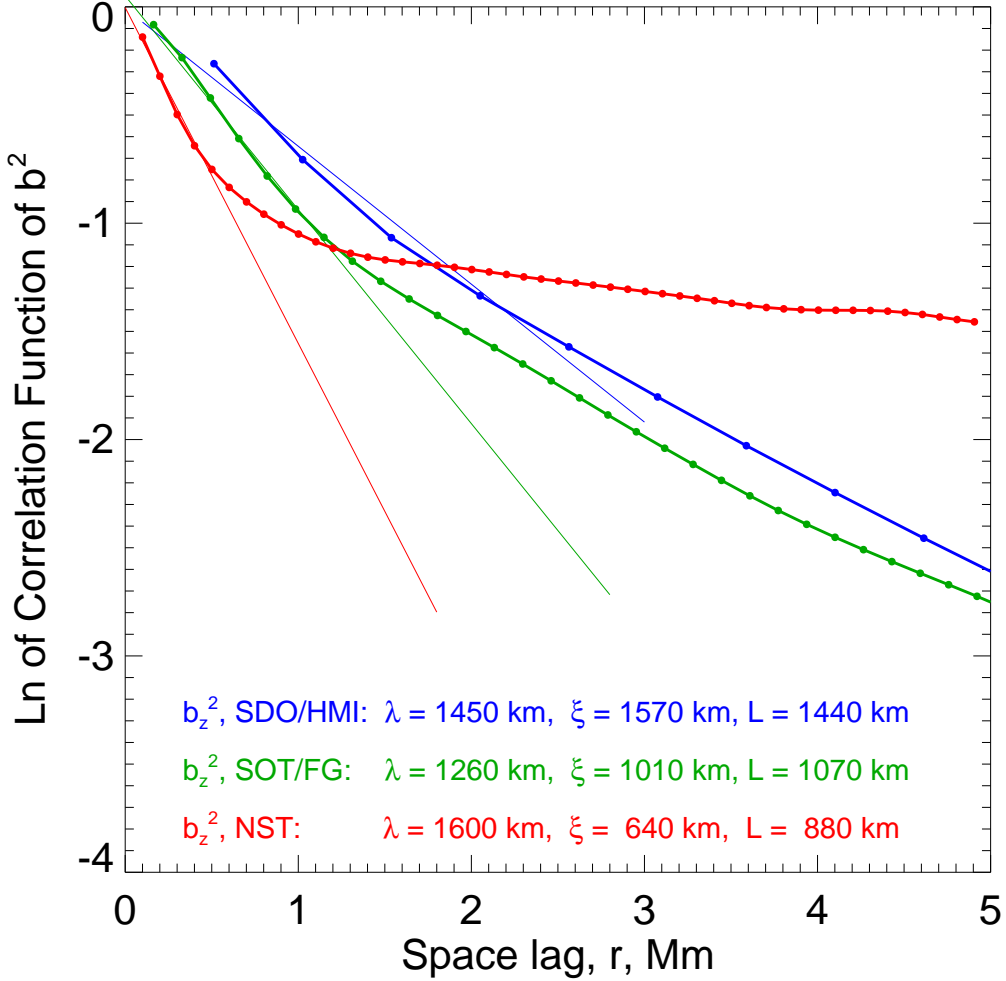


Fig. 9.— Plot of the natural logarithm of the correlation function of  $b_z^2$  versus the spatial lag  $r$  for the same area on the Sun (the CH 2011-08-12) but derived from data acquired with different instruments. The notation is the same as in Figure 8.

When comparing the characteristic lengths derived for  $u^2$  with those derived for  $b_t^2$ , we find that for the integral length  $\lambda(u^2)/\lambda(b_t^2) \approx 1.2$  for the correlation length  $\zeta(u^2)/\zeta(b_t^2) \approx 1.3$  and for the  $e$ -folding length  $L(u^2)/L(b_t^2) \approx 1.7$ . Thus, the characteristic scale of the squared velocity fluctuations is larger than that of the squared transverse magnetic field.

In Figure 9, we compare the  $b_z^2$ -correlation functions derived from magnetic field data ob-



tained with SDO/HMI (pixel scale 0."5), *Hinode* SOT/FG (pixel scale 0."16), and NST/IRIM (pixel scale 0."098) instruments for the same area inside the CH-2011-08-12. The figure demonstrates that the correlation function becomes narrower and produces smaller estimates of the characteristic length as the spatial resolution improves.

## 6. Conclusions and Discussion

Using high spatial (0."1) and temporal (12-13 s) resolution time series of solar granulation acquired inside two CHs with the NST at BBSO, we computed the characteristic (correlation) length of the transverse velocity fluctuations  $u^2$ . The corresponding length of the transverse magnetic field fluctuations  $b_t^2$  was derived from a unique and high quality *Hinode* SOT/SP data set which covered a large area of  $220 \times 120$  Mm.

The characteristic length of the energy containing structures  $u^2$  and  $b_t^2$  was derived from correlation functions of  $u^2$  and  $b_t^2$  by using three independent methods. These were calculated from the Batchelor integral scale  $\lambda$ , the correlation length  $\varsigma$ , and the  $e$ -folding length  $L$ .

For  $u^2$ -structures, Batchelor integral scale  $\lambda$  varies in the range of 1800 - 2100 km, whereas values of  $\varsigma$  and  $L$  vary between 660 and 1460 km. The structures for  $b_t^2$  yield Batchelor integral scale as  $\lambda \approx 1600$  km, a correlation length as  $\varsigma \approx 640$  km, and an  $e$ -folding length as  $L \approx 620$  km. The averaged (over  $\lambda$ ,  $\varsigma$ , and  $L$ ) characteristic scale for the  $u^2$ -fluctuations is  $1260 \pm 500$  km, and that for  $b_t^2$  is  $950 \pm 560$  km.

The above results show that the characteristic length derived from squared velocity fluctuations exceeds that derived from the squared transverse magnetic field fluctuations by 20 - 70%.

By analyzing the correlation functions of the velocity components  $u_x$  and  $u_y$ , we found that the normal and parallel correlation functions are different. For the case of isotropic hydrodynamical turbulence  $B_p(r) > B_n(r)$ , whereas the correlation functions observed here are in the opposite sense, i.e.,  $B_p(r) < B_n(r)$  at all observable scales. The discrepancy might be attributed to the presence of the magnetic field and/or violation of the isotropy. The parallel correlation function yields a characteristic length for the velocity fluctuations of  $803 \pm 157$  km, whereas the characteristic length derived from the normal correlation function is  $1307 \pm 278$  km.

As the spatial resolution improves, the correlation function for  $b_z^2$  becomes narrower and yields smaller estimates of the characteristic length. Since the correlation functions of  $b_z^2$  and  $b_t^2$  are similar, one might expect that with improved solar instruments,  $b_t^2$  might well produce smaller estimates for  $\lambda_{\perp}$ . Thus, we may perhaps regard the magnitudes of  $\lambda_{\perp}$  reported here as an upper

limit only.

Certainly, the study described here warrants further investigation using better magnetic field data. For example, the velocity and transverse magnetic field measurements should refer to a CH area, whereas in this study, the transverse magnetic field fluctuations were obtained for a quiet sun region. However, we may be obtaining realistic estimates because, as it is shown in Figure 8, the correlation functions for CH and the quiet sun areas are rather similar and produce similar estimates of the characteristic length. It would be also useful to compare the LCT results with those derived from the tracking of magnetic elements. This task requires high cadence and a long series of magnetic fields measured inside CHs, and is left for a future study.

We have shown that the characteristic length of the energy-containing structures in the photosphere lies in the range of 600-2000 km, which is on average an order of magnitude lower than the values used currently in models (e.g., Matthaeus et al. 1999; Dmitruk et al. 2001). Taking into account that the nonlinear dissipation terms in the MHD equations (Eq.(1) in Zank et al. (2012)), is inversely proportional to the correlation length of energy containing structures at the base of the corona (see Eq.16 in Zank et al. (2012)), our results here play a critical role in determining the effectiveness of the coronal turbulence transport models in heating the solar corona and hence in driving the solar wind.

It is worthy to note that obtained estimates of the averaged transverse velocity (about  $1.2 \text{ km s}^{-1}$ ) and the characteristic length scale for  $u^2$ -fluctuations (about 1300 km), combined with the results of Rüdiger et al. (2011) allowed us to evaluate the turbulent magnetic diffusivity and cross-helicity in the photosphere. Indeed, when the above estimates are used in the expression for turbulent magnetic diffusivity  $\eta_T \approx u_{rms}l/3$ , it gives us  $\eta_T \approx 500 \pm 200 \text{ km}^2 \text{ s}^{-1}$  ( $5 \times 10^{12} \text{ cm}^2 \text{ s}^{-1}$ ). In turn, the cross-helicity, according to Eqs. 19,24 in Rüdiger et al. (2011), is in direct proportion with  $\eta_T$ . This allows us to conclude that the magnitude of the cross-helicity ( $1 \text{ G km s}^{-1}$ ) obtained by Rüdiger et al. (2011) with  $\eta_T = 1 \times 10^{12} \text{ cm}^2 \text{ s}^{-1}$ , might be at least five times larger. The importance of the cross-helicity for estimation of internal solar parameters needed for dynamo was emphasized by Kuzanyan et al. (2007) and Pipin et al. (2011).

It is interesting that the magnitude of the turbulent magnetic diffusivity obtained here in a CH for the spatial scale of  $\sim 1300 \text{ km}$  coincides with the value of  $\eta_T$  inferred from the spectrum of the turbulent diffusion coefficient in a CH on scale of 1000-1300 km ( $460\text{-}560 \text{ km}^2 \text{ s}^{-1}$ ), reported by Abramenko et al. (2011, see Fig. 10 there). Thus, our present results indirectly support the previous inference that the turbulent diffusivity is a scale-dependent parameter. Additionally, the agreement between two independent estimates of  $\eta_T$  argues for the reliability of the LCT technique.

We thank the anonymous referee, whose careful reading and comprehensive reports with

critical comments significantly improved the paper. We are thankful to Dr. B. Lites for offering the processed SOT/SP data, to Drs. B. Vazquez, D. Hathaway, C. Smith for helpful discussion of these results. BBSO team efforts were supported by NSF (AGS-1146896, and ATM-0847126), NASA (NNX11AO73G), and AFOSR (FA9550-12-1-0066) grants.

## REFERENCES

- Abramenko, V. I., Carbone, V., Yurchyshyn, V., Goode, P. R., Stein, R. F., Lepreti, F., Capparelli, V., & Vecchio, A. 2011, *ApJ*, 743, 133
- Abramenko, V. I., Yurchyshyn, V. B., Goode, P. R., Kitiashvili, I. N., & Kosovichev, A. G. 2012, *ApJ*, 756, L27
- Batchelor. 1953, *The Theory of Homogeneous Turbulence* (Cambridge: Cambridge University Press)
- Berdyugina, S. V., Solanki, S. K., & Frutiger, C. 2003, *A&A*, 412, 513
- Bogdan, T. J., et al. 2003, *ApJ*, 599, 626
- Cao, W., Ahn, K., Goode, P. R., Shumko, S., Gorceix, N., & Coulter, R. 2011, in *Astronomical Society of the Pacific Conference Series*, Vol. 437, *Solar Polarization 6*, ed. J. R. Kuhn, D. M. Harrington, H. Lin, S. V. Berdyugina, J. Trujillo-Bueno, S. L. Keil, & T. Rimmele, 345
- Cao, W., Gorceix, N., Coulter, R., Ahn, K., Rimmele, T. R., & Goode, P. R. 2010, *Astronomische Nachrichten*, 331, 636
- Chae, J., & Sakurai, T. 2008, *ApJ*, 689, 593
- Cranmer, S. R., & van Ballegoijen, A. A. 2005, *ApJS*, 156, 265
- Cranmer, S. R., van Ballegoijen, A. A., & Edgar, R. J. 2007, *ApJS*, 171, 520
- Denker, C., Tritschler, A., Rimmele, T. R., Richards, K., Hegwer, S. L., & Wöger, F. 2007, *PASP*, 119, 170
- Dmitruk, P., Milano, L. J., & Matthaeus, W. H. 2001, *ApJ*, 548, 482
- Feder, J. 1989, *Fractals* (New York and London: Plenum Press)
- Freytag, B., Steffen, M., Ludwig, H.-G., Wedemeyer-Böhm, S., Schaffenberger, W., & Steiner, O. 2012, *Journal of Computational Physics*, 231, 919

- Goode, P. R., Cao, W., Ahn, K., Gorceix, N., & Coulter, R. 2011, in *Astronomical Society of the Pacific Conference Series*, Vol. 437, *Solar Polarization 6*, ed. J. R. Kuhn, D. M. Harrington, H. Lin, S. V. Berdyugina, J. Trujillo-Bueno, S. L. Keil, & T. Rimmele, 341
- Goode, P. R., Yurchyshyn, V., Cao, W., Abramenko, V., Andic, A., Ahn, K., & Chae, J. 2010, *ApJ*, 714, L31
- Hinze. 1959, *Turbulence: An Introduction to Its Mechanism and Theory* (New York: McCraw-Hill)
- Hurlburt, N. E., Schrijver, C. J., Shine, R. A., & Title, A. M. 1995, in *ESA Special Publication*, Vol. 376, *Helioseismology*, 239
- Jenkins, & Watts. 1969, *Spectral analysis and its applications* (San Francisco, Cambridge, London, Amsterdam: HOLDEN-DAY)
- Kosugi, T., et al. 2007, *Sol. Phys.*, 243, 3
- Kuzanyan, K. M., Pipin, V. V., & Zhang, H. 2007, *Advances in Space Research*, 39, 1694
- Lites, B. W., et al. 2008, *ApJ*, 672, 1237
- Matloch, Ł., Cameron, R., Shelyag, S., Schmitt, D., & Schüssler, M. 2010, *A&A*, 519, A52
- Matthaeus, W. H., Zank, G. P., Oughton, S., Mullan, D. J., & Dmitruk, P. 1999, *ApJ*, 523, L93
- Monin, A., & Yaglom, A. 1975, *Statistical Fluid Mechanics: Mechanics of Turbulence* (Cambridge: Cambridge: MIT Press)
- November, L. J., & Simon, G. W. 1988, *ApJ*, 333, 427
- Oughton, S., Matthaeus, W. H., & Zank, G. P. 1999, in *ESA Special Publication*, Vol. 446, 8th SOHO Workshop: *Plasma Dynamics and Diagnostics in the Solar Transition Region and Corona*, ed. J.-C. Vial & B. Kaldeich-Schü, 525
- Pipin, V. V., Kuzanyan, K. M., Zhang, H., & Kosovichev, A. G. 2011, *ApJ*, 743, 160
- Rüdiger, G., Kitchatinov, L. L., & Brandenburg, A. 2011, *Sol. Phys.*, 269, 3
- Stein, R. 2013, private communication
- Strous, L. 1994, PhD thesis, Utrecht University, The Netherlands
- Strous, L. H., Scharmer, G., Tarbell, T. D., Title, A. M., & Zwaan, C. 1996, *A&A*, 306, 947

- Thomas, J. H., & Stanchfield, I. D. C. H. 2000, *ApJ*, 537, 1086
- Title, A. M., Hurlburt, N., Schrijver, C., Shine, R., & Tarbell, T. 1995, in *ESA Special Publication*, Vol. 376, *Helioseismology*, 113
- Tsuneta, S., et al. 2008, *Sol. Phys.*, 249, 167
- Verdini, A., Velli, M., Matthaeus, W. H., Oughton, S., & Dmitruk, P. 2010, *ApJ*, 708, L116
- Verma, M., & Denker, C. 2011, *A&A*, 529, A153
- Verma, M., Steffen, M., & Denker, C. 2013, *ArXiv e-prints*
- Wang, J., Wang, H., Spirock, T., Lee, C., Ravindra, N., Ma, J., Goode, P., & Denker, C. 2000, in *SPIE*, Vol. 4093, *Current Developments in Lens Design and Optical Systems Engineering*, ed. W. H. Swantner, R. E. Fischer, R. B. Johnson, & W. J. Smith, 481
- Welsch, B. T., et al. 2007, *ApJ*, 670, 1434
- Wöger, F., & von der Lühe, O. 2007, *Appl. Opt.*, 46, 8015
- Zank, G. P., Dosch, A., Hunana, P., Florinski, V., Matthaeus, W. H., & Webb, G. M. 2012, *ApJ*, 745, 35